

# Optimization of regional constraints for estimating the Greenland mass balance with GRACE level-2 data

Z. Xu, E. Schrama and W. van der Wal

*Faculty of Aerospace Engineering, Delft University of Technology, the Netherlands. E-mail: Z.Xu-1@tudelft.nl*

Accepted 2015 March 30. Received 2015 March 27; in original form 2014 October 1

## SUMMARY

Data from the Gravity Recovery and Climate Experiment (GRACE) satellite mission can be used to estimate the mass change rate for separate drainage systems (DSs) of the Greenland Ice Sheet (GrIS). One approach to do so is by inversion of the level-2 spherical harmonic data to surface mass changes in predefined regions, or mascons. However, the inversion can be numerically unstable for some individual DSs. This occurs mainly for DSs with a small mass change signal that are located in the interior region of Greenland. In this study, we present a modified mascon inversion approach with an improved implementation of the constraint equations to obtain better estimates for individual DSs. We use separate constraints for mass change variability in the coastal zone, where run-off takes place, and for the ice sheet interior above 2000 m, where mass changes are smaller. A multi-objective optimization approach is used to find optimal prior variances for these two areas based on a simulation model. Correlations between adjacent DSs are suppressed when our optimized prior variances are used, while the mass balance estimates for the combination of the DSs that make up the GrIS above 2000 m are not affected significantly. The resulting mass balance estimates for some DSs in the interior are significantly improved compared to an inversion with a single constraint, as determined by a comparison with mass balance estimates from surface mass balance modelling and discharge measurements. The rate of mass change of the GrIS for the period of January 2003 to December 2012 is found to be  $-266.1 \pm 17.2 \text{ Gt yr}^{-1}$  in the coastal zone and areas below 2000 m, and  $+8.2 \pm 8.6 \text{ Gt yr}^{-1}$  in the interior region.

**Key words:** Inverse theory; Satellite gravity; Time variable gravity; Glaciology; Arctic region.

## 1 INTRODUCTION

The Gravity Recovery and Climate Experiment (GRACE) mission was launched in March 2002. Several studies have shown that ice mass decrease takes place on Greenland using data from the GRACE mission, (Schrama *et al.* 2011; Jacob *et al.* 2012; Sasgen *et al.* 2012; Shepherd *et al.* 2012; Barletta *et al.* 2013; Luthcke *et al.* 2013; Velicogna & Wahr 2013; Schrama *et al.* 2014). An advantage of satellite gravimetry is that one can directly derive the total ice mass balance after correcting for glacial isostatic adjustment and atmospheric, oceanic and continental hydrology mass changes. An alternative method is to measure surface elevation change by satellite altimetry, in which case the density of the snowpack, the firn and the deeper ice must be known to estimate the mass change of an ice sheet. A drawback of satellite gravity measurements is the relatively low spatial resolution compared to satellite altimetry measurements (Zwally *et al.* 2005). The nature of satellite gravity in combination with the post-processing is such that leakage effects can be seen in the maps of gravity change as a result of the signal

spreading outside the source region (Velicogna & Wahr 2005; Chen *et al.* 2007).

In order to deal with GRACE measurement error and leakage effects different approaches have been suggested. By means of averaging kernels, *cf.* Velicogna & Wahr (2005) and Swenson & Wahr (2007), one can minimize the combined GRACE measurement error and leakage effects to derive an average mass change for the GrIS or for larger subregions of the GrIS. Velicogna & Wahr (2005) assume an averaging function that is computed under the assumption of uniform mass change distributed in the coastal zone and zero in the interior of Greenland. However, several studies have indicated that neither the mass change in the coastal zone is evenly distributed nor mass change in the interior of Greenland is zero (Johannessen *et al.* 2005; van den Broeke *et al.* 2009). Furthermore, the averaging function for the GrIS extends to the neighbouring land areas of northern Canada where mass changes also occur (Luthcke *et al.* 2013).

The mass concentration (mascon) methods described in Luthcke *et al.* (2006, 2013) and Rowlands *et al.* (2010) result in mass changes

for a global set of mascons directly from the K-band ranging data from the GRACE satellites (the so-called level-1b data) and from information on the orbit of the GRACE satellites determined by GPS tracking and accelerometer measurements. In Luthcke *et al.* (2013) the mascons are taken to be  $1^\circ \times 1^\circ$  blocks. In order to suppress leakage and signal loss as a result of filtering, this approach considers GRACE data with the full GRACE noise covariance. The study of Luthcke *et al.* (2013) considers anisotropic constraints for neighbouring mascons, and it assumes separate GrIS regions below and above 2000 m. It is shown by Luthcke *et al.* (2013) that for smaller areas, that is for 34 subregions of the GrIS, meaningful regional mass changes still can be revealed from the GRACE data when proper constraints are introduced.

Other studies have estimated regional mass changes from the GRACE level-2 potential coefficients. Wouters *et al.* (2008) (hereafter W08) implement a forward modelling approach similar to the mascon layout used by Luthcke *et al.* (2013) whereby a fixed number of basin-shaped regions on the GrIS are considered. For a discussion about the definition of GrIS basins see Rignot & Kanagaratnam (2006). Scaling factors for each region are adjusted iteratively to find a best match between the equivalent water heights obtained from GRACE and their equivalent that follows from the forward model used by W08. Regional mass changes from this approach match the results from the mascon method described in Luthcke *et al.* (2006) as well as other studies (Sasgen *et al.* 2012; Shepherd *et al.* 2012). A least-squares inversion approach described in Schrama & Wouters (2011; hereafter SW11) also employs the basin shaped mascons, but it is different from the forward method as in W08, since the least-squares approach is introduced. This approach improves the effectiveness of the approach of W08 by reducing the required computing power. SW11 show that the approximated regional mass balance agrees with the results retrieved via the mascon method in eight major GrIS drainage basins.

The least-squares inversion approach described in SW11 leads to correlation between adjacent regions. An increase in mass loss in one region can be compensated by mass gain in adjacent regions so that the overall mass balance is unchanged. We will address the correlation effect in Section 2 but here we discuss two solutions to this problem which are given in SW11. The first is that the solution becomes more stable when several adjacent regions are combined into a single estimate. The second solution is to implement regularization in the least-squares estimation (Tikhonov 1963), which means that the approximations of the regional mass changes are constrained by prior information. This solution is also referred to as constrained least-squares adjustment (SW11). With the second approach, the question is which values should be used as constraint. When the constraints are too tight the regional mass change estimates are biased towards *a priori* information. On the other hand the instability can remain in regions if the constraint is too loose. SW11 applied a loose constraint by assuming that the prior variance imposed on each basin is less than  $10^6$  relative to the variance of the EWT observation. In SW11 several basin configurations were considered for the GrIS. The 13 basin configuration where the area above 2000 m on the GrIS was taken as one mascon was preferred in that study because the inter-region correlation was suppressed compared to the 20-basin solution.

To determine the optimal prior variances for the 20-region configuration, Bonin & Chambers (2013; hereafter BC13) implemented the constrained least-squares approach assuming one prior variance (referred to as process noise in their study) for 16 GrIS subareas and one for mascons in the surrounding ocean as well as in northern Canada. In BC13, the constraint variance is optimized by means of

a simulation model based on the annual elevation change rate found by Zwally *et al.* (2005). However, according to BC13, the mass changes estimated for some regions still contain noticeable errors. We will discuss these errors when applying the same optimal prior variance as constraint in Section 2. Thus a single constraint for all regions in Greenland yields suboptimal results in least-squares inverted GRACE level 2 data. Another study of constraining the inversion approach using simulation is that of Baur & Sneeuw (2011), in which point masses are used instead of basin shaped mascons. In Baur & Sneeuw (2011), the approximation norm and the residual norm associated with a series of constraint are compared in an L-curve (Hansen 1992) and the one in the 'corner' of the L-curve is considered to be the optimal.

The goal of this paper is to build on SW11 and BC13 and to investigate whether an alternative constraint model for the basin-shaped mascons can be justified that results in improved mass change estimates for individual regions

The inversion modelling approach from SW11 is described in Section 2. We improve the regional mass balance approximation, in particular in the GrIS interior, by assuming separate constraints for regions above and below 2000 m. Optimal prior variances for different regions are found by applying the inversion approach to simulated monthly mass changes over the GrIS. In this simulation approach, discussed in Section 3, we rely on RACMO2 model output (Ettema *et al.* 2009) and satellite radar interferometry observations of the ice discharge (Rignot & Kanagaratnam 2006). In Section 4, we will introduce an optimization procedure for prior variances for different GrIS regions by searching for the optimal combinations using a genetic algorithm. In Section 5, we will apply the optimal prior variances in the least-squares inversion modelling approach, and discuss the effect on regional mass changes from GRACE level-2 data. The conclusions are summarized in Section 6.

## 2 INVERSE MODELLING OF GRIS REGIONAL MASS CHANGES

The GRACE derived monthly geopotential changes are represented by potential coefficients. In Wahr *et al.* (1998) it is shown how monthly geopotential changes can be converted into surface mass changes expressed in water equivalent thickness under the assumption that one takes away the effects of tides, air pressure loading, mass changes in the ocean, and glacial isostatic adjustment. The inverse modelling approach used here aims at representing the equivalent water changes that follow from Wahr *et al.* (1998) by average water equivalent changes in predefined regions within the GrIS and the surrounding areas.

A sensible choice for obtaining predefined regions is to divide the GrIS into regions according to their natural drainage system (DS). Here we follow the definition of the DS described in Zwally *et al.* (2011) so that we arrive at an 8-region layout (Fig. 1). In addition we divide each DS at the 2000 m elevation contour, with the interior region being the one above 2000 m, cf. Thomas *et al.* (2001), W08, SW11 and BC13. SW11 compared multiple layouts for the GrIS as well as the surrounding regions which are Ellesmere island, Baffin island, Iceland and Svalbard (EBIS). When considering the GrIS as one single region SW11 found a mass loss of  $-150 \text{ Gt yr}^{-1}$  between 2003 and 2010. Their conclusion was that a single mascon results in underestimated mass changes for the GrIS compared to other studies using GRACE data (Sasgen *et al.* 2012; Shepherd *et al.* 2012). The accuracy of the approximation in SW11 was improved by applying a 20-region setup which separated the GrIS into 8 DS each divided in

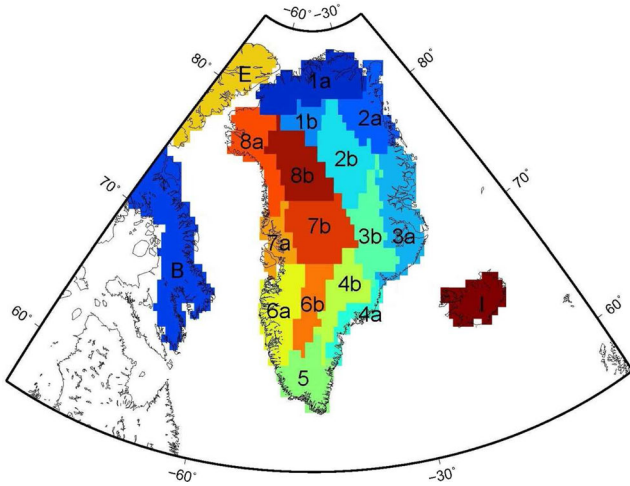


**Figure 1.** Drainage system divides according to Zwally *et al.* (2012). The digits are the ID's of the drainage basins. The subregion is marked by the character after the decimal. The characters 'a' and 'b' refer to the GrIS margin and interior regions, respectively. Note that in this figure Svalbard is not displayed but it is included in the 19-region layout.

a region above and below 2000 m elevation. EBIS areas were treated as four separate regions as well. With this configuration SW11 found an annual mass loss rate of around  $-250 \text{ Gt yr}^{-1}$  which agrees with other studies. So when using the least-squares inversion approach, it is also possible to approximate the GrIS mass changes in small regions while providing reasonable estimates of the mass change for the whole GrIS. However, when using the GRACE level-2 potential coefficients, the spatial resolution is limited by the maximum degree and order. In this study, we use the CSR GRACE coefficients that are truncated at maximum degree and order 60. Therefore regional mass balances derived from these truncated GRACE level 2 data should not rely on subregions that are too small. In this study we will use the same amount of subregions as SW11. Moreover, compared to other region layouts, as described in Luthcke *et al.* (2013), we use a more conservative 2000 m divide. The GRACE EWT map used in this study has a resolution of  $1^\circ$  which is close to a  $110 \times 110 \text{ km}$  square on the equator. In our layout, a grid cell is considered as interior only if 80 per cent of the area of the grid cell has an altitude higher than 2000 m. We find that only six cells in DS 5 are above 2000 m, so in our layout we chose not to separate DS 5. W08 and SW11 found that the mass changes above the GrIS observed by GRACE contain leakage from the EBIS areas which is the reason for including these areas in the inversion. Overall, as depicted in Fig. 1, we define 15 GrIS regions and four EBIS regions.

In order to implement the method, we first assume a uniformly distributed water layer with unit thickness within each region, that is  $f_k(\theta, \lambda) = 1$  when  $[\theta, \lambda]$  is within the domain of the region and 0 outside, where the subscript  $k = 1, 2, 3, \dots, n$  indicates each region. We convert the mass distribution  $f_k$  into potential coefficients up to degree and order 60 which are filtered by an isotropic Gaussian filter as described in Swenson & Wahr (2002) with half width  $r_{1/2} = 300 \text{ km}$ . Then we convert the coefficients to EWT in the spatial domain and order the values as a column vector, which becomes the influence function  $g_k(f_k)$ . Both SW11 and BC13 have discussed the consequences of using different half widths in the inversion approach. A half width of  $r_{1/2} = 300 \text{ km}$  was found in SW11 and BC13 to be the best compromise (compared to 0, 500 and 700 km) between suppressing the noise in GRACE data and being able to compute mass changes in our configuration of regions.

We construct a matrix  $\mathbf{H} = [g_1, g_2, \dots, g_n]$  and a vector of scaling factors  $\mathbf{x} = [a_1, a_2, \dots, a_n]^T$  associated with the assumed mass distribution  $f_k$ , so that:

$$\mathbf{y} = \mathbf{H}\mathbf{x} + \boldsymbol{\varepsilon} \quad (1)$$

The vector  $\boldsymbol{\varepsilon}$  contains the misclosures between the observations  $\mathbf{y}$  and the model  $\mathbf{H}\mathbf{x}$ .  $\mathbf{y}$  contains the global mass changes ordered as a column vector, which in this study is either derived from the simulation model (see Section 3) or from the GRACE observations (see Section 5). The best approximation can be found by minimizing the sum of the squared residuals. To do so, we solve eq. (1) using a least-squares approach. As in SW11, we define the cost function for the least-squares approach as

$$J = \boldsymbol{\varepsilon}^T \boldsymbol{\varepsilon} \quad (2)$$

the minimization of which yields, under the assumption of a uniform variance of all observations in the vector  $\mathbf{y}$ ,

$$\hat{\mathbf{x}} = (\mathbf{H}^T \mathbf{H})^{-1} \mathbf{H}^T \mathbf{y} \quad (3)$$

Eq. (3) is an unconstrained solution because no other information was considered than the observations. As a result, the residuals are minimized for the entire GrIS but the solution is numerically unstable. The numerical instability manifests itself in the form of anticorrelation between neighbouring regions so that we can see the typical high-low-high patterns as demonstrated by BC13, also *cf.* Baur & Sneeuw (2011). Such a pattern will be called anticorrelation error in the following. One way to deal with this problem is to average the mass changes in the anticorrelated neighbouring regions, for example by combining the area above and below 2000 m in one DS (Sasgen *et al.* 2012) or by combining the interior regions *cf.* SW11. Although the errors are reduced by combining regions, they still exist in sub-areas. For instance, in SW11, when separating each drainage area by the 2000 m elevation contour, the approximated mass balance of the entire GrIS is obtained with a relatively low uncertainty, that is  $-201.4 \pm 21.0 \text{ Gt yr}^{-1}$  during 2003–2010. However the uncertainties for separated GrIS margin and interior areas became larger, that is  $-263.3 \pm 55.6$  and  $62.0 \pm 46.5 \text{ Gt yr}^{-1}$ , respectively.

The regional instability can be reduced by introducing prior variances as constraints on the mass changes for each region, also known as the Tikhonov regularization (Tikhonov 1963). Note that in general Tikhonov regularization,  $\mathbf{P} = \lambda \mathbf{R}$  where  $\mathbf{R}$  is the regularization matrix and  $\lambda$  is the regularization parameter. In this study we assume that in the prior matrix, all the regions are equally weighted, yielding  $\mathbf{R} = \mathbf{I}$ . Also we use the prior variance  $\sigma^2$  of the regional mass variations in each regions as the regularization parameter so that the constraint can be written as  $\mathbf{P} = \sigma^2 \mathbf{I}$ , and the cost function becomes:

$$J = (\boldsymbol{\varepsilon}^T \boldsymbol{\varepsilon} + \mathbf{x}^T \mathbf{P}^{-1} \mathbf{x}) \quad (4)$$

where the residual norm  $\boldsymbol{\varepsilon}^T \boldsymbol{\varepsilon}$  is associated with the observations with unit weight and the approximation norm  $\mathbf{x}^T \mathbf{P}^{-1} \mathbf{x}$  contains the prior information. With this information we restrict the variance of the regional scaling factor  $\mathbf{x}$ , in order to reduce the anticorrelation errors, *cf.* SW11. In this case eq. (3) becomes:

$$\hat{\mathbf{x}} = (\mathbf{H}^T \mathbf{H} + \mathbf{P}^{-1})^{-1} \mathbf{H}^T \mathbf{y} \quad (5)$$

All regions are considered to have the same prior variance in SW11 and BC13. However, it has been found in BC13 that with the optimized prior variance  $\sigma^2$ , the anticorrelation still remained in some oversensitive regions that have a higher than average mass change per grid cell. For instance, in DS 6, the area of the coastal



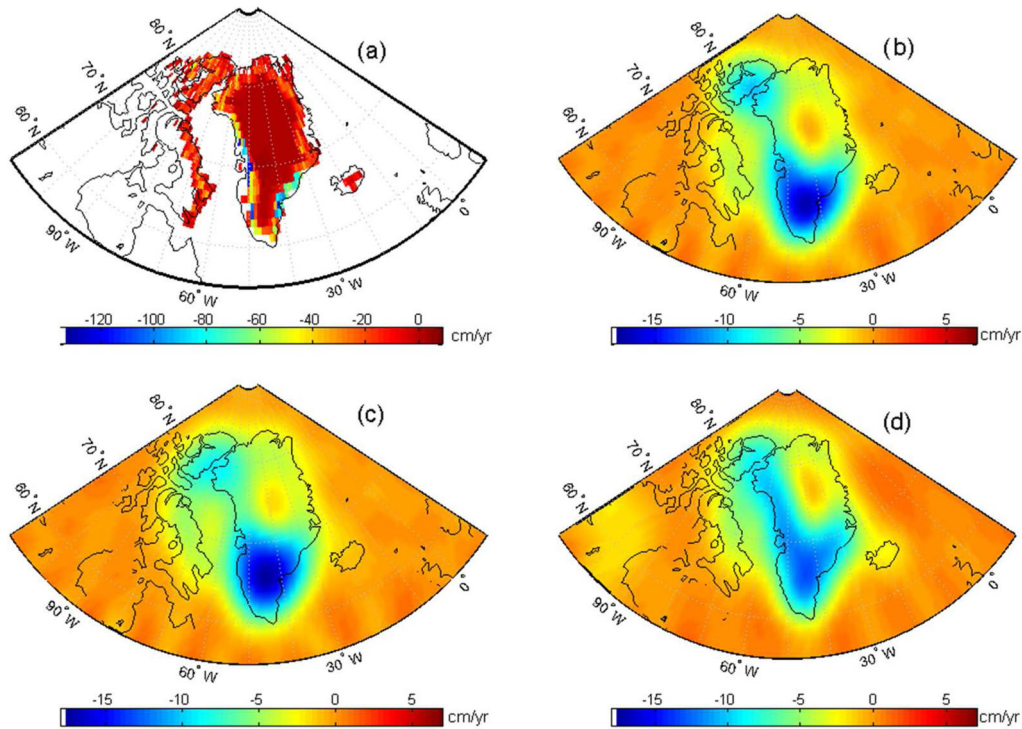


**Figure 2.** Mass change simulation model results based on the IOM. (a) shows the gridded EWT change trend on a  $1^\circ \times 1^\circ$  grid for the time period January 2003 to April 2012. The unit is  $\text{cm yr}^{-1}$ . Panel (b) shows EWT change trend of the simulation model  $\mathbf{y}$ . The simulation is based on (a) after spherical harmonic analysis and synthesis up to degree and order 60 and Gaussian filtering ( $r_{1/2} = 300$  km), and also includes noise in the GRACE data. The average EWT change trend for each region computed from the IOM is  $\mathbf{x}'$ , and the associated simulated GRACE data (after smoothing)  $\mathbf{y}' = \mathbf{H}\mathbf{x}'$  is shown in (c). Panel (d) shows the annual EWT trend retrieved from the GRACE data for the same time span.

region is around  $1.6 \times 10^5 \text{ km}^2$  and for the interior region it is around  $1.2 \times 10^5 \text{ km}^2$ . In these two similar sized regions, the mass change rates are significantly different. According to the modelling of the surface mass balance, the mass changes in this interior region are smaller than in the margin region (Ettema *et al.* 2009; Fettweis *et al.* 2011). Also in the same DS, from GRACE data, Luthcke *et al.* (2013) found a much lower mass change rate in the interior and much more mass loss near the margin by using the direct mascon approach with geolocatable constraints for the mascons below and above 2000 m. However, when applying the same constraint as in BC13, the mass change estimates for DS 6 from GRACE data were  $-8.9 \pm 4$  and  $-9.8 \pm 3.7 \text{ Gt yr}^{-1}$ , for the margin and for interior regions, respectively. So the mass balance approximations in both regions are likely in error because the interior region should lose less mass than the margin because run-off is smaller. BC13 quantified this type of error with a simulation method and found that in DS 6, when using the same optimal constraint the regional mass estimates were anticorrelated, and the associated error was  $-8.4 \text{ Gt yr}^{-1}$  for the GrIS margin area and  $+11.2 \text{ Gt yr}^{-1}$  for the interior region. Hence in order to further improve the least-squares approximation in regions, the constraint  $\mathbf{P}$  matrix will be composed of a group of non-identical prior variances. In our case an optimal  $\mathbf{P}$  is based on a full time-series simulation model which will be described in Section 3.

### 3 SIMULATION OF THE GRIS MASS BALANCE

In this section, we introduce a simulation model that produces a reasonable representation of monthly mass changes on Greenland

and its surrounding areas so that optimal prior constraint variances can be determined. For this purpose we use the RACMO2 model and discharge data to simulate 108 months (January 2003 to April 2012) of surface mass changes on the spatial domain with a resolution of  $1^\circ \times 1^\circ$ . RACMO2 estimates the SMB by modelling the regional precipitation, runoff, refreezing and evaporation/sublimation and is accurate to within  $\sim 18$  per cent, according to Sasgen *et al.* (2012). To compute the total mass balance for Greenland we also use ice discharge data that have been derived from SAR data (Rignot & Kanagaratnam 2006) to yield a discharge mass flux at the glacier boundary. The remaining areas of the world are set to zeroes. This model describes the mass conservation of GrIS and will be referred to as Input-Output Model (IOM) in the following *cf.* Shepherd *et al.* (2012).

In Fig. 2(a), the IOM output is in the form of the gridded annual EWT change rate for Greenland and the surrounding EBIS regions. We convolve the gridded mass distribution over the Earth's surface and obtain the potential coefficients in response to this distribution up to degree  $l = 60$ .

Additionally, the noise in GRACE level-2 data potentially increases the variability of the monthly regional mass balance. Therefore we also simulate the GRACE noise by applying the approach of BC13. In this approach the noise is isolated from the GRACE data by removing from it all known components, including the continental hydrology, all the glacier regions and GIA, using the following external information:

- (1) The model output from the Global Land Data Assimilation System (Rodell *et al.* 2004; GLDAS) using the Noah Land Surface Model.

- (2) Annual mass changes on land glaciers outside the GrIS from Jacob *et al.* (2012).
- (3) The GrIS regional mass changes from Sasgen *et al.* (2012).
- (4) The GIA model of Paulson *et al.* (2007).

This information is converted into monthly potential coefficients complete up to degree and order 60 and removed from GRACE potential coefficients. From the remaining coefficients, a covariance matrix is constructed, which is subsequently used to generate random potential coefficients according to the procedure in appendix A of BC13. In this study, we simulate the GRACE noise for every month, then add it to the potential coefficients of the IOM model. We apply a Gaussian filter with a smoothing radius  $r_{1/2} = 300$  km on the combined coefficients and calculate the EWT map for the complete simulation model. The simulation model in terms of annual EWT change is shown in Fig. 2(b).

Due to the uncertainty in the RACMO2 and discharge estimates, there will be regional differences between the simulation model and GRACE observations as can be seen in Figs 2(b) and (d), but we use the simulation only as a reasonable mass change signal to derive constraints. In the next section, we will use the above described simulation model to optimize the prior covariance matrix  $\mathbf{P}$  in our inversion algorithm.

#### 4 OPTIMIZATION OF THE CONSTRAINTS IN LEAST-SQUARES APPROACH

In order to find the optimal priori covariance matrix  $\mathbf{P}$ , we apply eq. (5), replacing  $\mathbf{y}$  by simulated data. Since  $\hat{\mathbf{x}}$  is supposed to represent the average regional mass balances, we compare them to the regionally averaged simulated data without noise, being just the IOM model output averaged by region (see Fig. 2c). To distinguish from the simulated data we label the regionally averaged IOM model output with  $\mathbf{y}'$ . Note that the GRACE noise is not included in  $\mathbf{y}'$ .

##### 4.1 Optimization of constraint

The optimal constraint covariance matrix  $\mathbf{P}$  is achieved when the differences between the approximation  $\mathbf{H}\hat{\mathbf{x}}$  and the averaged model  $\mathbf{y}'$  reaches a minimum. Using eq. (5) the difference is a function of the prior covariance matrix  $\mathbf{P}$ :

$$f(\mathbf{P}) = \mathbf{y}' - \mathbf{H}(\mathbf{H}^T\mathbf{H} + \mathbf{P}^{-1})^{-1}\mathbf{H}^T\mathbf{y}. \quad (6)$$

Note that eq. (6) is different from the cost function in eq. (4) for the least-squares inversion, because  $\mathbf{y}'$  contains only the regionally averaged IOM model output, which means that  $f(\mathbf{P})$  is different from the residual  $\epsilon$  in eq. (1) and eq. (2).

BC13 considered a uniform prior variance factor  $\sigma^2$  for all regions to form the  $\mathbf{P}$  matrix (which we denote as constraint matrix  $\mathbf{P}_1$ ), so that  $\sigma_1^2 = \sigma_2^2 = \dots = \sigma_n^2 = \sigma^2$  and  $\mathbf{P}_1 = \sigma^2\mathbf{I}$ . Here we consider different variances on the diagonal of the  $\mathbf{P}$  matrix. We use the notation  $\mathbf{P}_3$  to define our  $\mathbf{P}$  matrix because we define 3 prior variances factors. To form the  $\mathbf{P}_3$  matrix, for the regions below 2000 m we define the associated prior variance elements as  $\sigma_{1\dots 8}^2 = \sigma_d^2$ . For the regions above 2000 m, a different prior variance is applied, i.e.  $\sigma_{9\dots 15}^2 = \sigma_u^2$ , and we use  $\sigma_{16\dots 19}^2 = \sigma_{EBIS}^2$  to describe the prior variance of the EBIS areas.

We evaluate eq. (6) and take the root-mean-square (rms) difference to the simulation as the first objective function:

$$G_1 = \sqrt{\frac{\int_{\Omega} f^2(\mathbf{P})}{A}}, \quad (7)$$

where  $\Omega$  defines the area which we use for comparison, between  $40^\circ$ – $85^\circ$ N and  $255^\circ$ – $385^\circ$ W, and  $A$  is the total surface area of  $\Omega$ .

Since the evaluation is based on the trend difference during the simulated time span, it only describes the long-term behaviour of the mass change rate in each region. As discussed in W08 and BC13, the inter-region correlation should also be taken into account for assessing the quality of approximated solutions. Hence, we introduce a second objective function during the optimization:

$$G_2 = \sqrt{\frac{\sum_{i,j=1}^n (r_{ij}^2 - \hat{r}_{ij}^2)^2}{n^2}}. \quad (8)$$

It is the rms of the difference between the inter-region correlation coefficient matrix for the simulation model  $\mathbf{R} = [r_{ij}^2]$  and the inter-region correlation coefficient matrix for the approximation  $\hat{\mathbf{R}} = [\hat{r}_{ij}^2]$ , where  $r_{ij}^2$  and  $\hat{r}_{ij}^2$  are the correlation coefficients between the time series of approximated monthly regional mass changes in region  $i$  and region  $j$  from 2003 to 2012, in the simulation and the approximation, respectively. They state the correlation in monthly mass changes between two regions.  $n$  is the total number of mascon regions in the least-squares inversion. Examples of the inter-region correlation can be found in Fig. 5, which will be discussed in Section 4.5.

##### 4.2 Evaluation of objective functions

First, we evaluate the objective function eqs (7) and (8) using *a priori* covariance matrix  $\mathbf{P}_1$  as the constraint where varies  $\sigma^2$  from 0.001 to 1000  $\text{m}^2$ . We find that when  $\sigma^2 = 1000 \text{ m}^2$  the influence of  $\mathbf{P}_1$  on the approximation in eq. (5) becomes negligible, so that an unconstrained approximation is obtained. The corresponding rms difference of the EWT trend  $G_1 = 0.44 \text{ cm}$ . For  $\sigma^2 < 1 \text{ m}^2$   $G_1$  is larger than the unconstrained solution thus these variances are rejected. The objective function as a function of the prior variance is shown in Fig. 3(a). As can be seen in this figure, the minimum of the objective function  $G_1 = 0.35 \text{ cm}$  is achieved when  $\sigma^2 = 3 \text{ m}^2$ . However, we find the minimum of the inter-region correlation difference,  $G_2 = 0.44$ , when  $\sigma^2 = 5 \text{ m}^2$ . Also when we gradually increase the value of  $\sigma^2$  from 3 to 5  $\text{m}^2$ , the evaluation of  $G_1$  diverges from the minimum while the evaluation of  $G_2$  is converging towards to its minimum. Thus, there is a trade-off between these two objective functions within the range where the optimal  $\sigma^2$  is mostly likely to be found. In this study, in order to choose from two values for the prior variance which both yield the optimal scores but for different objective functions, we assess the overall return when altering the solution. For instance we chose  $\sigma^2 = 5 \text{ m}^2$  as the optimal solution for  $\mathbf{P}_1$ , because when comparing to  $\sigma^2 = 3 \text{ m}^2$ ,  $G_2$  is reduced by 6 per cent while  $G_1$  is increased by only 1 per cent. One may argue that the differences are small. However, the objective functions  $G_1$  and  $G_2$  are computed as spatial averages, and when the averaged difference is integrated over the indicated region with a total area of approximately  $2.6 \times 10^7 \text{ km}^2$ , significant differences can be found. We will discuss the spatial differences in Section 4.4.

The optimization process becomes more complicated when  $\mathbf{P}_3$  is used as the constraint covariance matrix, since the dimension of the search space of  $\mathbf{P}_3$  increases by 2 compared to  $\mathbf{P}_1$ . Manually

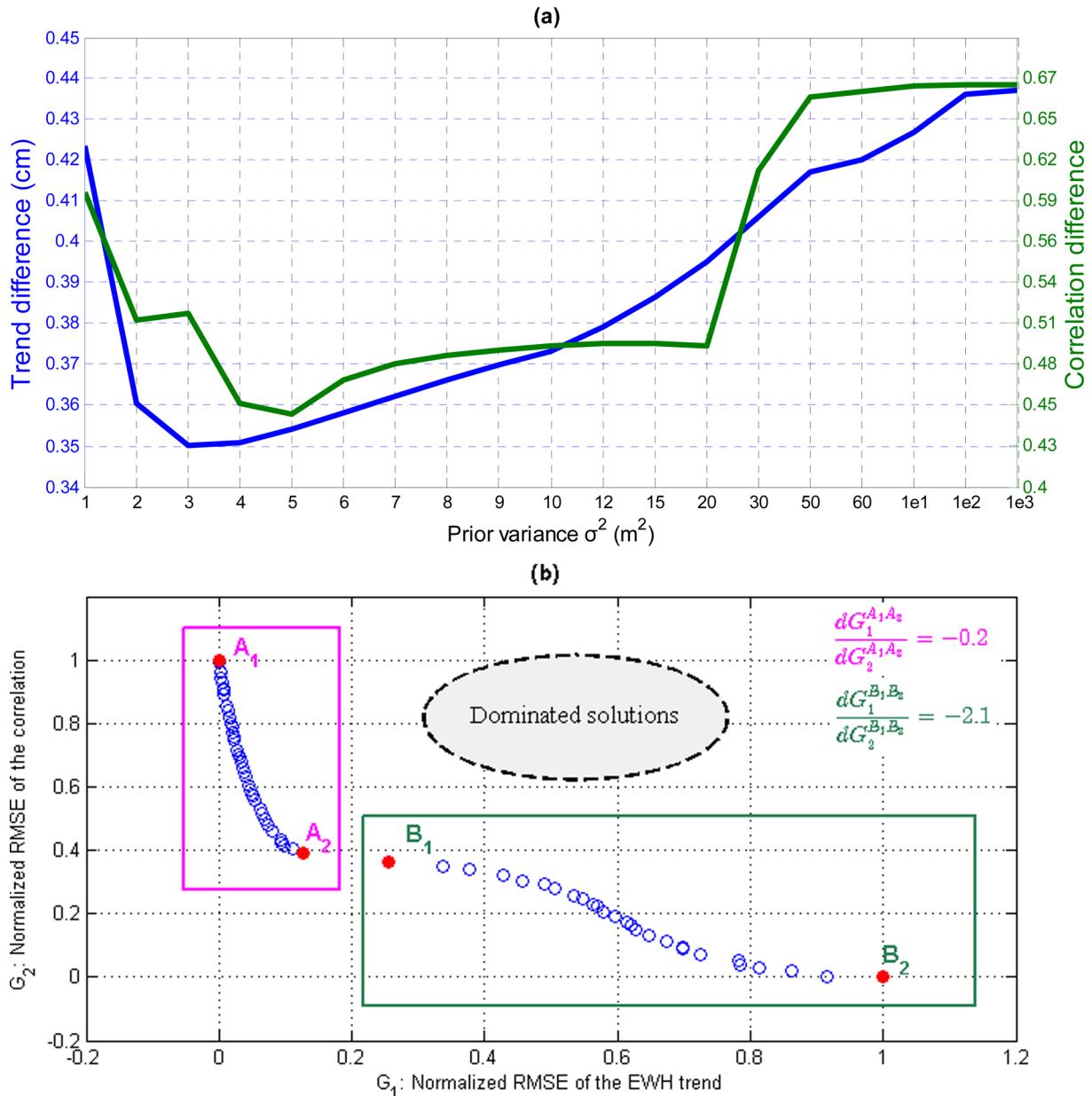


**Figure 3.** (a) The blue line shows the rms differences in the annual trend between the approximated solution and the simulation model, that is the objective function  $G_1$ . The green line shows the objective function  $G_2$  which is the rms difference of the inter-region correlation matrix for the simulation and for the approximation. Panel (b) shows the performance of all the dominating solutions  $P_3$  (blue circles) along the Pareto front with respect to the objective functions  $G_1$  (x-axis) and  $G_2$  (y-axis). The values are normalized to a range of 0–1. The dominating solutions are categorized into two groups, the dominating solutions in the pink box are better for the objective function  $G_1$ ; the green box contains the solutions that yield a smaller objective function  $G_2$ . For each box, we compute the slope of the vector from the upper-left point to the bottom right point, marked by solid red circles.

testing each possible  $P_3$  to locate the minimum with both objective functions turns out to be time consuming. For this reason we employ a genetic algorithm (GA) technique, the Non-Dominating Sorting Genetic Algorithm (NSGA-II; Deb *et al.* 2002), that is built-in the Matlab optimization toolbox, version 2012. NSGA-II is a fast multi-objective optimization algorithm that is designed to find the optimal solution in case there are multiple objectives that need to be minimized/maximized and also allows easy extension of the method to more than three prior constraints. NSGA-II iteratively evaluates and updates the solution. In GA the term population is defined as a group of solutions each consisting of different combinations of variables. In this study these variables are the variance factors in

$P_3$ . In the NSGA-II algorithm the population is evaluated at every iteration through the objective functions, and the populations are ranked based on the outcome. The NSGA-II algorithm ranks the population by applying the ‘non-domination’ rule. If an individual is worse than at least one other individual regarding all the objectives, then it is dominated by those individuals. Individuals which are not dominated by any others are the dominating individuals and the collection of the dominating individuals is the Pareto front. For instance, in Fig. 3(a) when using the covariance matrix  $P_1$  as the constraint and letting  $\sigma^2 = 3, 5$  and  $20 \text{ m}^2$ , we find that  $G_1$  is 0.35, 0.36 0.40 cm and  $G_2$  is 0.51, 0.45, 0.49, respectively. The solution  $\sigma^2 = 20 \text{ m}^2$  yields the largest approximation error in both objective



functions, so it is a dominated solution and will not be selected. Although  $\sigma^2 = 3 \text{ m}^2$  is a better solution than  $\sigma^2 = 5 \text{ m}^2$  regarding the cost function  $G_1$ , the opposite is true when considering the cost function  $G_2$ . So  $\sigma^2 = 3 \text{ m}^2$  and  $\sigma^2 = 5 \text{ m}^2$  are both dominating solutions. In NSGA-II, during every generation, the individuals on the Pareto fronts are given the top rank, while the individuals on the second best front are given the second rank, and so on. NSGA-II repeats this process until the entire population in the current generation is ranked.

Individuals with parents with high rank will provide the information used for creating a new population in the next generation, also referred to as children. For instances, if the covariance matrix  $\mathbf{P}_i^t$  and  $\mathbf{P}_j^t$  are the parents at generation  $t$ , then in generation  $t+1$ , NSGA-II will create a new  $\mathbf{P}^{t+1}$  which is identical to either  $\mathbf{P}_i^t$  or  $\mathbf{P}_j^t$  in part of the dimensions. In addition, we apply a mutation in one or more of the dimensions during the process of generating children, in order to avoid the solutions converging to a local minimum or maximum. NSGA-II will stop when it reaches the maximum specified number of generations. We also restrict the value of  $\sigma$  in  $\mathbf{P}_3$  to fall in the range  $[0.001, 1000]$ . Moreover, we define the size of population to be 100 and the maximum number of generations to be 50. During the optimization, we found that the size of the population and the maximum number of generations is sufficient to find the global optimum. The final Pareto front, consisting of 70 different cases of  $\mathbf{P}_3$ , is shown in Fig. 3(b) in which the evaluations of the objective functions are normalized to a range of 0–1. After normalization, the minimum and maximum evaluations of  $G_1$  and  $G_2$  become 0 and 1, respectively.

In Fig. 3(b) it can be observed that these solutions naturally fall into two distinguishable categories. The solutions within the pink box show a small change in the normalized objective function  $G_1$ , but a large change in the normalized cost function  $G_2$ . Two points in this group that yield the local minimum in either  $G_1$  or  $G_2$  are shown by solid red circles, that is  $A_1$  and  $A_2$ . For  $G_1$  the scores of these two points are  $G_1^{A1} = 0$  and  $G_1^{A2} = 0.13$ . On the other hand, the evaluations of  $G_2$  are  $G_2^{A1} = 1$  and  $G_2^{A2} = 0.4$ . The slope of the normalized vector  $\vec{A_1A_2}$  is around  $-0.2$ , which indicates that if we chose  $A_2$  over  $A_1$ , we gain 1 unit improvement in  $G_2$  while losing 0.2 unit of  $G_1$ . Because of the relatively small increase in  $G_1$ , we choose the solution  $\mathbf{P}_3$  associated with the point  $A_2$  to be the local optimal solution in this group.

Similarly, for another group, we identify the boundary points  $B_1$  and  $B_2$  inside the green box, with scores of  $G_1^{B1} = 0.23$  and  $G_1^{B2} = 1$ ,  $G_2^{B1} = 0.38$  and  $G_2^{B2} = 0$ . The slope of the normalized

vector  $\vec{B_1B_2}$  is  $-2.0$ , which means that when we move from point  $B_1$  to point  $B_2$ , in order to reduce  $G_2$  by 1 unit we will increase  $G_1$  by 2.0 units. Regarding the overall return  $B_1$  is a better than  $B_2$  in this group. Thus, we have found two local optimal solutions for  $\mathbf{P}_3$ ,  $A_2$  and  $B_1$ . If we select  $B_1$  over  $A_2$ ,  $G_2$  is reduced by only 0.02 while  $G_1$  is increased by 0.2. Thus  $A_2$  is selected to be the optimal point, and the associated solution is  $\mathbf{P}_3$  with the diagonal elements  $[10.0, 0.1, 1.9] \text{ m}^2$ .

### 4.3 Trend differences

This section discusses the differences between the approximated simulation and the simulation, or  $G_1$  in eq. (7). Note that we do not consider the uncertainty in the RACMO2 and discharge data when we use them to create the simulation model as a reasonable benchmark. The actual uncertainty of the simulation model is discussed in Section 6. The errors in the simulation and approximated simulation only reflect the uncertainty caused by linear interpolation for a 95 per cent confidence interval.

In the simulation model a mass change of  $-249.7 \pm 4.9 \text{ Gt yr}^{-1}$  is found for the entire GrIS (15 regions) from January 2003 to April 2012. The mass change trends from the approximation are  $-242.2 \pm 4.3 \text{ Gt yr}^{-1}$ ,  $-247.5 \pm 4.3 \text{ Gt yr}^{-1}$  and  $-251.2 \pm 4.3 \text{ Gt yr}^{-1}$  when the least-squares inversion approach is unconstrained and constrained using the optimal  $\mathbf{P}_1$  and constrained using the optimal  $\mathbf{P}_3$ , respectively. All three approximations are similar for the whole GrIS, however the differences between regional mass change trends are significant.

In Fig. 4, we compare the EWT rate differences between the approximations and the simulation model. We find that the differences are spatially anticorrelated. For example, in Fig. 4(a) where the approximation is the unconstrained solution, one can see underestimated mass loss rate in the west coastal regions. To compensate the insufficient mass loss, the least-squares approach increases the mass loss in adjacent regions, which leads to overestimated mass loss in the neighbouring Baffin island region and overestimated mass gain in the adjacent interior regions (both result in negative differences). This manifestation of the anticorrelation error during the least-squares inversion can be quantified by comparing with the simulation model. In Table 1 we find that the annual mass change trend in region 6a and 7a (margin of western GrIS) is  $-52.9 \pm 1.7$  and  $-16.6 \pm 0.4 \text{ Gt yr}^{-1}$  in the simulation model, whereas the unconstrained least-squares solution gives  $-64.3 \pm 1.9$  and  $-32.1 \pm 0.4 \text{ Gt yr}^{-1}$ , respectively. Inland we can see from this table a

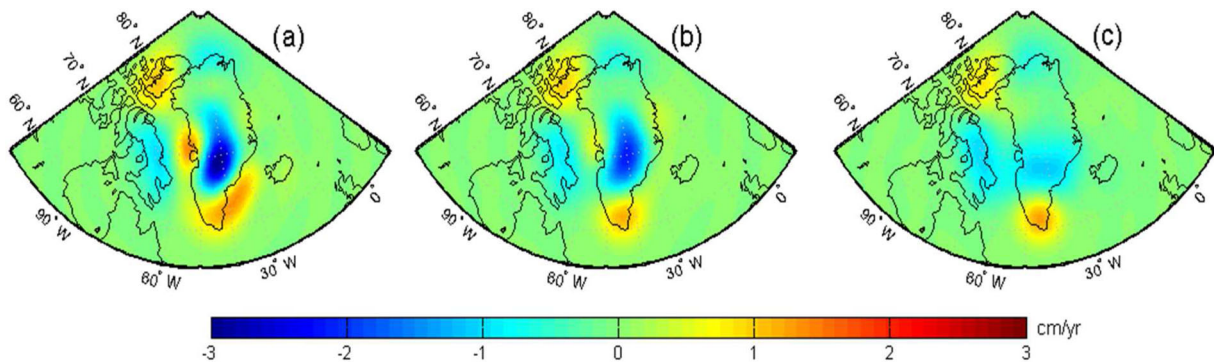


**Figure 4.** The linear trend of the approximated solutions after least-squares inversion minus the trend from the simulation (based on the RACMO2 model output and the discharge data). Three strategies are used for the constraints. (a) Unconstrained, (b) using the optimal  $\mathbf{P}_1$  as constraint and (c) using the optimal  $\mathbf{P}_3$  as the constraint. The unit is cm per year.

**Table 1.** The trend in monthly mass changes for all regions in  $\text{Gt yr}^{-1}$ . The uncertainties only refer to the uncertainty caused by linear interpolation for a 95 per cent confidence interval. For some regions, the uncertainty is 0.0 due to rounding. ‘IOM’ refers to the solutions derived from the IOM model, and the symbol ‘P’ means that no constraint is applied. Similarly,  $\mathbf{P}_1$  and  $\mathbf{P}_3$  indicate the scenarios in which the optimal prior covariance matrix  $\mathbf{P}_1$  and  $\mathbf{P}_3$  are applied, respectively. Note that the mass changes rates in this table refer to the time span from 2003 to 2012.

	GrIS region layout (Zwally <i>et al.</i> 2012)							
	DS 1	DS 2	DS 3	DS 4	DS 5	DS 6	DS 7	DS 8
	Region 1a	Region 2a	Region 3a	Region 4a	Region 5	Region 6a	Region 7a	Region 8a
IOM	$-23.7 \pm 0.5$	$-10.6 \pm 0.5$	$-34.3 \pm 0.7$	$-62.4 \pm 1.1$	$-32.1 \pm 0.6$	$-52.9 \pm 1.7$	$-16.6 \pm 0.4$	$-26.0 \pm 1.2$
P	$-11.6 \pm 0.3$	$-12.1 \pm 0.6$	$-25.4 \pm 0.6$	$-86.4 \pm 1.0$	$-30.1 \pm 0.6$	$-64.3 \pm 1.9$	$-32.1 \pm 0.4$	$-28.4 \pm 0.9$
$\mathbf{P}_1$	$-18.9 \pm 0.3$	$-11.4 \pm 0.6$	$-30.0 \pm 0.6$	$-72.0 \pm 0.8$	$-33.2 \pm 0.6$	$-51.0 \pm 1.7$	$-23.9 \pm 0.3$	$-28.9 \pm 0.9$
$\mathbf{P}_3$	$-21.2 \pm 0.4$	$-11.6 \pm 0.6$	$-31.9 \pm 0.6$	$-62.0 \pm 0.9$	$-34.8 \pm 0.6$	$-49.3 \pm 1.9$	$-18.3 \pm 0.4$	$-29.8 \pm 1.0$
	Region 1b	Region 2b	Region 3b	Region 4b		Region 6b	Region 7b	Region 8b
IOM	$0.4 \pm 0.1$	$3.0 \pm 0.1$	$0.7 \pm 0.1$	$0.3 \pm 0.1$		$1.0 \pm 0.3$	$2.8 \pm 0.2$	$0.8 \pm 0.1$
P	$-7.6 \pm 0.1$	$3.2 \pm 0.3$	$-4.5 \pm 0.1$	$19.5 \pm 0.4$		$17.1 \pm 0.4$	$12.2 \pm 0.2$	$7.9 \pm 0.3$
$\mathbf{P}_1$	$-3.8 \pm 0.1$	$3.0 \pm 0.2$	$3.5 \pm 0.1$	$5.0 \pm 0.1$		$2.1 \pm 0.2$	$9.0 \pm 0.2$	$3.1 \pm 0.2$
$\mathbf{P}_3$	$-0.1 \pm 0.0$	$2.2 \pm 0.1$	$0.6 \pm 0.0$	$0.4 \pm 0.0$		$0.5 \pm 0.0$	$3.2 \pm 0.0$	$0.9 \pm 0.0$
EBIS regions				Combined areas				
	Svalbard island	Elsmere island	Baffin island	Iceland	$\leq 2000$ m	$\geq 2000$ m	GrIS	GrIS $\pm$ EBIS
IOM	$-1.2 \pm 0.3$	$-36.0 \pm 1.2$	$-47.2 \pm 1.4$	$-6.0 \pm 0.2$	$-258.7 \pm 4.7$	$9.0 \pm 0.6$	$-249.7 \pm 4.9$	$-340.1 \pm 5.5$
P	$-0.5 \pm 0.3$	$-29.8 \pm 1.0$	$-51.7 \pm 1.5$	$-4.4 \pm 0.1$	$-290.2 \pm 4.5$	$47.8 \pm 0.6$	$-242.4 \pm 4.3$	$-328 \pm 5.0$
$\mathbf{P}_1$	$-0.4 \pm 0.3$	$-30.5 \pm 1.0$	$-50.6 \pm 1.4$	$-3.6 \pm 0.1$	$-269.4 \pm 4.2$	$21.8 \pm 0.5$	$-247.5 \pm 4.3$	$-332.6 \pm 9.4$
$\mathbf{P}_3$	$-0.4 \pm 0.3$	$-29.4 \pm 1.0$	$-49.3 \pm 1.4$	$-3.0 \pm 0.1$	$-258.8 \pm 4.4$	$7.6 \pm 0.1$	$-251.2 \pm 4.3$	$-333 \pm 4.9$

considerable mass gain in the approximation for both region 6b and region 7b, that is  $17.1 \pm 0.4$  and  $12.2 \pm 0.2$   $\text{Gt yr}^{-1}$  while in the simulation model there is only  $1.0 \pm 0.3$  and  $2.8 \pm 0.2$   $\text{Gt yr}^{-1}$  mass gain in regions 6b and region 7b, respectively.

When we use the optimal  $\mathbf{P}_1$  as constraint, and compare the EWT differences in Fig. 4(b), we find that the approximated mass change rate for the western coastal regions and the interior regions are closer to the simulation model, see Table 1. However, anticorrelation errors still exist in the interior. For instance, in region 7a and 7b the differences with respect to the simulation are  $-7.3$  and  $6.2$   $\text{Gt yr}^{-1}$ .

Apparently, one can easily cancel the errors by combining DS number 7a and 7b. However, this lowers the resolution of the approximation, so we apply the optimal  $\mathbf{P}_3$  matrix as constraint instead. After introducing a specific constraint for the interior regions with the optimal  $\mathbf{P}_3$  matrix, one can clearly see that the EWT rate differences with respect to the simulation model, Fig. 4(c), are reduced compared to Fig. 4(b), although the approximated mass change rates are still higher in region 7b and lower in region 7a. However, the error in this DS with respect to the simulation value is reduced to 10 per cent in the margin and 14 per cent in the interior.

The benefits of applying the constraint  $\mathbf{P}_3$  can also be seen when we combine all the regions above 2000 m. As shown in Table 1, in the simulation model the mass slowly accumulates during the time span with a rate of  $9.0 \pm 0.6$   $\text{Gt yr}^{-1}$ . This rate is poorly approximated with a value of  $47.8 \pm 0.2$   $\text{Gt yr}^{-1}$  when no constraint is used, and  $21.8 \pm 0.5$   $\text{Gt yr}^{-1}$  when the constraint  $\mathbf{P}_1$  is used. Our main conclusion is that we obtain the best approximated rate of  $7.6 \pm 0.1$   $\text{Gt yr}^{-1}$  for the combined interior regions when using  $\mathbf{P}_3$ .

#### 4.4 Inter-region correlation of the monthly mass balance

We also assess the approximations by comparing the inter-region correlations. As in eq. (8), we compute the correlation coefficient matrix  $\mathbf{R}$  of the monthly regional mass change approximations using different constraints. In Fig. 5, we plot the inter-region correlation coefficients of matrix  $\mathbf{R}$ , with each pixel in these plots referring to

the correlation between the monthly mass changes for region  $i$  on the  $x$ -axis and region  $j$  on the  $y$ -axis.

As the baseline, we show the correlation coefficient matrix  $\mathbf{R}_{sim}$  from the simulation model in Fig. 5(a). One can notice from this plot that there are three different ‘blocks’ in the matrix  $\mathbf{R}$ : (1) the triangular block on the top left (2) the square block on the bottom left and (3) another triangle block on the bottom right. They contain the correlations between margin regions (block 1), the correlations between margin and interior regions (block 2) and the correlations between interior regions only (block 3). In the simulation model, we find that in block 1 all correlations are positive and have high values ( $\geq 0.6$ ). The regions above 2000 m are also positively correlated but some regions have relatively low correlation with some other interior regions, for instance  $r_{3b,8b} = +0.2$  and  $r_{1b,8b} = +0.8$ . In block 2, the correlations between regions below and above 2000 m are all negative. Since the run-off is absent from the interior regions, the mass is slowly accumulating in the interior regions in the simulation model, whereas in all the regions below 2000 m the mass is decreasing over time, cf. van den Broeke *et al.* (2009). In the following, we will show that we can obtain the same (positive/negative) correlation pattern by using separate constraints for the interior and coastal regions.

In Fig. 5(b)–(d) we compare matrix  $\mathbf{R}$  associated with the solutions which are unconstrained, constrained by  $\mathbf{P}_1$ , constrained by  $\mathbf{P}_3$ , respectively. Pattern errors are noticeable in the first two approximations. For instance, in plot b (unconstrained) we find that the approximated monthly mass balances in region 3b are positively correlated with all the margin regions and negatively correlated with the internal regions, which is opposite to the pattern that we find in plot a. Since we have considered the inter-region correlation as one of the objective functions in the optimization of  $\mathbf{P}_1$ , the incorrect correlation pattern in region 3b is solved, see Fig. 5(c). However the problem remains in region 1b. As in plot d, we have restored the correct sign for almost all the regional mass balance by using the constraint  $\mathbf{P}_3$ .

Nevertheless, one may argue that in spite of the sign of the correlation being correct in plot d, the values of the correlation



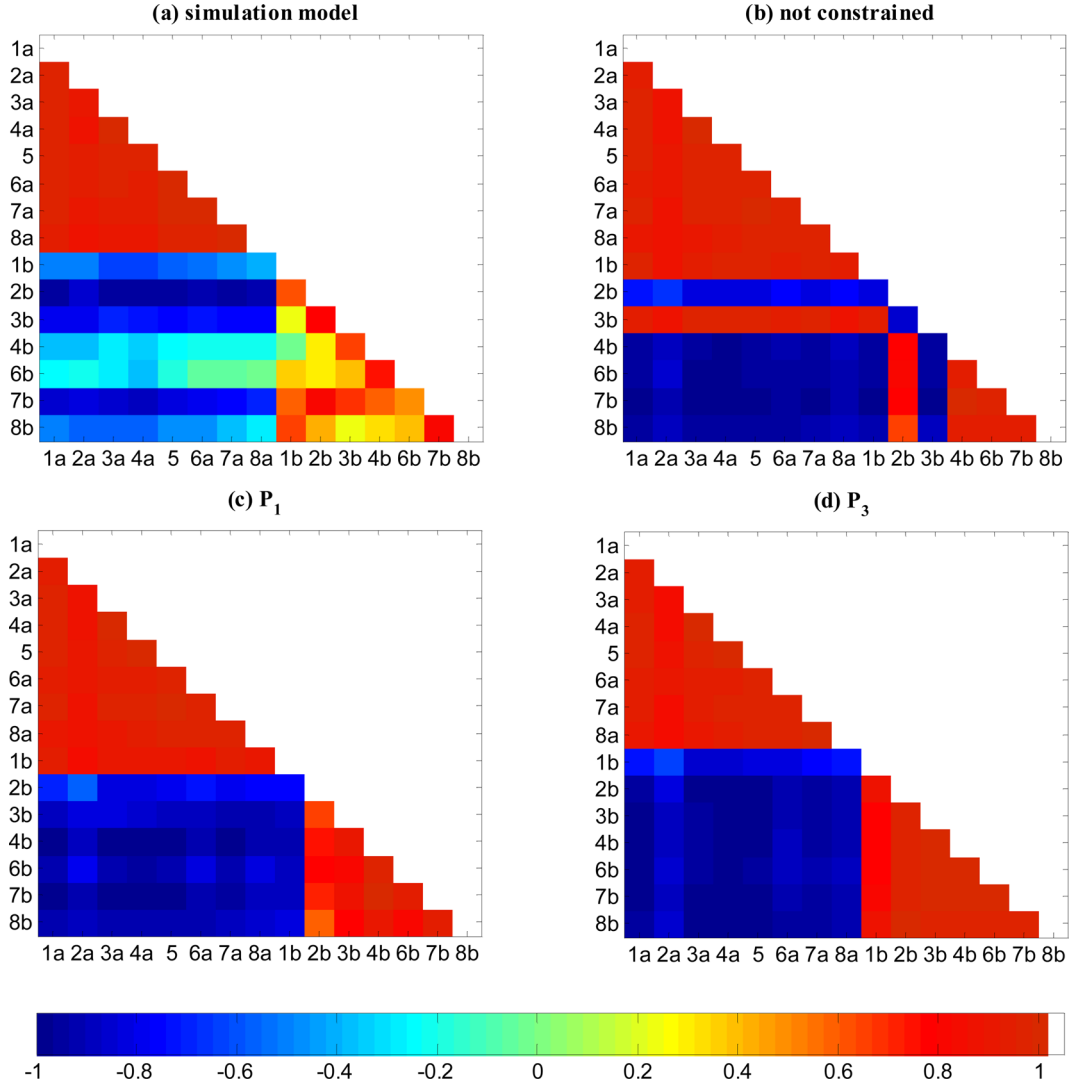


**Figure 5.** The correlation coefficients of monthly mass balance between the different regions. Each plot is derived from the simulated (a) or the approximated (b, c, d) monthly mass balances.

coefficients are different from the simulation. For instance, we find  $|r_{8a,6b}| = 0.02$  in the simulation model, which means that the mass balance in region 8a and in region 6b are not correlated. However in plot d the absolute correlation coefficient between these two regions becomes  $|r_{8a,6b}| = 0.89$ , thus the approximated correlation is much stronger. The correlation is also enhanced when applying the constraint  $P_1$  as well as in the unconstrained results. Despite the remaining inter-region correlation differences with respect to the simulation, we minimize the correlation difference by using optimal constraints based only on the objective function for the inter-region correlation. From Table 2 it is clear that we reduce the errors in the inter-region correlation using the optimal  $P_3$  as constraint. It might be possible to further reduced the incorrect correlation by introducing more constraints, which we leave to future work.

## 5 APPROXIMATE THE REGIONAL MASS CHANGES FROM GRACE DATA

In this section, we approximate the monthly mass changes in GRACE observations using the least-squares inversion approach with the optimal constraints  $P_1$  and  $P_3$ . We use the release 5 level

**Table 2.** The rms differences of the inter-region correlation between three approximations with different constraints and the simulation model. Block (1) refers to the correlation between regions below 2000 m. Block (2) refers to the correlation between regions below and above 2000 m and Block (3) refers to the correlation between regions above 2000 m.

	Not constrained	$P_1$	$P_3$
Block 1	0.17	0.11	0.11
Block 2	0.71	0.51	0.30
Block 3	0.78	0.63	0.33

2 GRACE monthly potential coefficients from CSR which have a maximum spherical harmonic degree 60. The time interval is January 2003 to December 2012, with a few months excluded because of insufficient observations (July 2003, January 2004, January 2011 and June 2011). We remove a mean over 2003 to 2012 to obtain monthly mass changes. GRACE data is less accurate in  $C_{20}$  (Chen *et al.* 2005 and Chen *et al.* 2011), hence we replace the  $C_{20}$

**Table 3.** Approximated annual trend from GRACE data using different constraints on combined areas. The unit is  $\text{Gt yr}^{-1}$ .

	Not constrained	$\mathbf{P}_1$	$\mathbf{P}_3$
<2000 m	$-272.3 \pm 17.4$	$-263.4 \pm 17.2$	$-266.1 \pm 17.2$
$\geq 2000$ m	$13.1 \pm 9.7$	$7.5 \pm 8.6$	$8.2 \pm 8.6$
GrIS	$-259.1 \pm 19.9$	$-255.9 \pm 19.2$	$-257.9 \pm 19.2$
EBIS	$-90.9 \pm 22.6$	$-87.2 \pm 22.1$	$-81.4 \pm 22.1$

coefficients with estimates from Satellite Laser Ranging (SLR) (Cheng *et al.* 2013). Since the orbit centre of GRACE satellites is identical to the instantaneous centre of mass of the Earth, degree 1 potential coefficients cannot be obtained from GRACE. We use the degree 1 coefficients provided by CSR, which are potential coefficients recovered using GRACE coefficients above degree 2 together with output from an ocean model (Swenson *et al.* 2008).

The mass changes on GrIS are also influenced by continental hydrology and the GIA effect. We use the monthly GLDAS-Noah model described in Rodell *et al.* (2004) to remove the continental hydrology leakage, and use the GIA model from Paulson *et al.* (2007) to correct for GIA. To reduce high-frequency noise and inter-coefficient correlation that manifests as so-called stripes (Swenson & Wahr 2006) we use a Gaussian filter (Wahr *et al.* 1998) with a half width of  $r_{1/2} = 300$  km, the same as used in simulation model. Potential coefficients are converted to monthly EWT changes in the spatial domain and the constrained least-squares inversion approach is applied with the optimal constraints  $\mathbf{P}_1$  and  $\mathbf{P}_3$ , to obtain an approximation of the GrIS monthly mass balances observed by the GRACE satellites.

We first assess the approximation in combined areas as shown in Table 3. Note that the estimated errors in the annual mass changes consist of the vector sum of (1) the standard deviations of the GRACE data which is also provided by CSR, (2) the estimated uncertainty of 20 per cent in the GIA model (Paulson *et al.* 2007) which is a guess of the inherent uncertainty in the implemented ice model ICE-5G (Peltier 2004) and (3) the estimated 30 per cent average uncertainty in the GLDAS-NOAH model (Fang *et al.* 2009). The uncertainty from estimating a linear trend with a 95 per cent confidence interval is considered as well. In Table 3, for the entire GrIS and for subregions, not using constraints or using  $\mathbf{P}_1$  and  $\mathbf{P}_3$  as constraint all yield consistent mass change trends. This indicates that the anticorrelation errors disappear when regions with negative correlation are combined.

In Fig. 6, one can observe that the anticorrelation errors are reduced using the optimal  $\mathbf{P}_3$ . For instance, in region 1b, when using the constraint  $\mathbf{P}_1$  the rate is  $10.8 \pm 5.5 \text{ Gt yr}^{-1}$  while in the neighbouring region 8b, the rate is  $-9.7 \pm 5.3 \text{ Gt yr}^{-1}$  which is significantly different. The difference is caused by the numerical instability of the inversion which manifests as anticorrelation between adjacent regions, because when comparing the values to the rates found with the RACMO2 model for the same time period, the two regions show similar mass changes rate, with  $0.4 \pm 0.1 \text{ Gt yr}^{-1}$  in region 1b and  $0.5 \pm 0.1 \text{ Gt yr}^{-1}$  in region 8b. Due to the fact that the run-off and ice discharge is absent in this area, the RACMO2 model output is more accurate there (Ettema *et al.* 2009). In order to improve the incorrectly distributed regional mass change between these two regions one can use the constraint  $\mathbf{P}_3$  in which case the rate becomes similar to RACMO2 model output, that is  $1.7 \pm 5.5$  and  $0.8 \pm 5.3 \text{ Gt yr}^{-1}$  in region 1b and region 8b, respectively.

When using the constrained least-squares approach, the approximated solution is determined by both the GRACE observation and

the simulation model. The mass balance of the interior regions is influenced by the external information in the form of  $\mathbf{P}_1$  or  $\mathbf{P}_3$ . Moreover, as in Fig 6(a), when considering the uncertainties of the rate estimation, we find that the approximations in most of the regions below 2000 m are consistent between the cases unconstrained, or optimal constraints for  $\mathbf{P}_1$  and  $\mathbf{P}_3$ . Hence during the least-squares inversion, the mass balance of these regions is not sensitive to changes in the constraints. Only in region 4a and region 7a, which are the GrIS margin regions located at the south east and west, we find that the rate estimations change by a value larger than the error bars when we alter the constraints. The sensitivity becomes more obvious for regions above 2000 m. For instance on region 2b, the rate difference between the solution using  $\mathbf{P}_1$  and the unconstrained solution is insignificant, ( $17.1 \pm 2.6 \text{ Gt yr}^{-1}$  compared to  $17.6 \pm 2.6 \text{ Gt yr}^{-1}$ ), whereas we obtain a much lower rate of  $5.4 \pm 2.6 \text{ Gt yr}^{-1}$  using  $\mathbf{P}_3$ . However, for region 7b, using  $\mathbf{P}_1$  and  $\mathbf{P}_3$  results in similar estimates of  $-0.3 \pm 4.3$  and  $0.6 \pm 4.4 \text{ Gt yr}^{-1}$  mass change, respectively, both of which are much lower than the rate of  $32.7 \pm 4.4 \text{ Gt yr}^{-1}$  from the unconstrained solution.

The constrained mass change rate derived from the GRACE data is similar to the IOM solution for the whole GrIS, that is  $-258 \pm 19$  and  $-249.7 \pm 34 \text{ Gt yr}^{-1}$ , respectively. However differences can be noticed in the southeast and northwest coastal regions. We compare the regional mass changes trend in the IOM (see Table 1) with the ones in the approximations from GRACE data (see Fig. 6). Note that in Table 1, the uncertainties for the IOM mass changes only refer to the uncertainties of the linear interpolation; the uncertainties in the RACMO2 model and the discharges estimations are considerably larger ( $\sim 20$  per cent, cf. Rignot *et al.* 2008; Ettema *et al.* 2009; Sasgen *et al.* 2012). In the southeast coastal region 4a, the IOM present more mass loss trend than in the approximations from GRACE data, that is  $-62$  and  $-52 \text{ Gt yr}^{-1}$ , while the difference can be explained by the large uncertainties ( $\sim 30$  per cent) of the surface mass balance model in this region (cf. Sasgen *et al.* 2012; Vernon *et al.* 2013; Andersen *et al.* 2015). In the northwest region 8a, when applying  $\mathbf{P}_3$  the mass change rate is  $-44.1 \text{ Gt yr}^{-1}$  from the GRACE data but only  $-26.0 \text{ Gt yr}^{-1}$  mass loss rate is given by the simulation. As it has been discussed by Sasgen *et al.* (2012), this difference can be caused by the high uncertainties of the discharge estimation in this region; the uncertainties in the simulation model for this region can be approximately 50 per cent. These regional differences to the IOM model are also seen in the GRACE inferred EWH map, as in Fig. 2. If we compare the GRACE data (without approximating the regional mass changes) to the IOM based simulation model, it also shows more mass loss in the northwest and less in the southeast. It indicates that although the optimized constraint is based on the simulation model, the approximations are still mainly determined by the observations.

## 6 DISCUSSION

Least-squares inversion of mass change rates on Greenland from GRACE data requires the use of constraints on the variance. It was shown by BC13 that the value of the constraint should be optimized, otherwise incorrect regional mass balance estimates can result. We build on their results and find that even the use of a single constraint can result in incorrect estimated mass changes for individual regions. The main problem is that in regions of small mass change, the inversion will place negative mass changes next to positive mass change. In our study we propose to use different

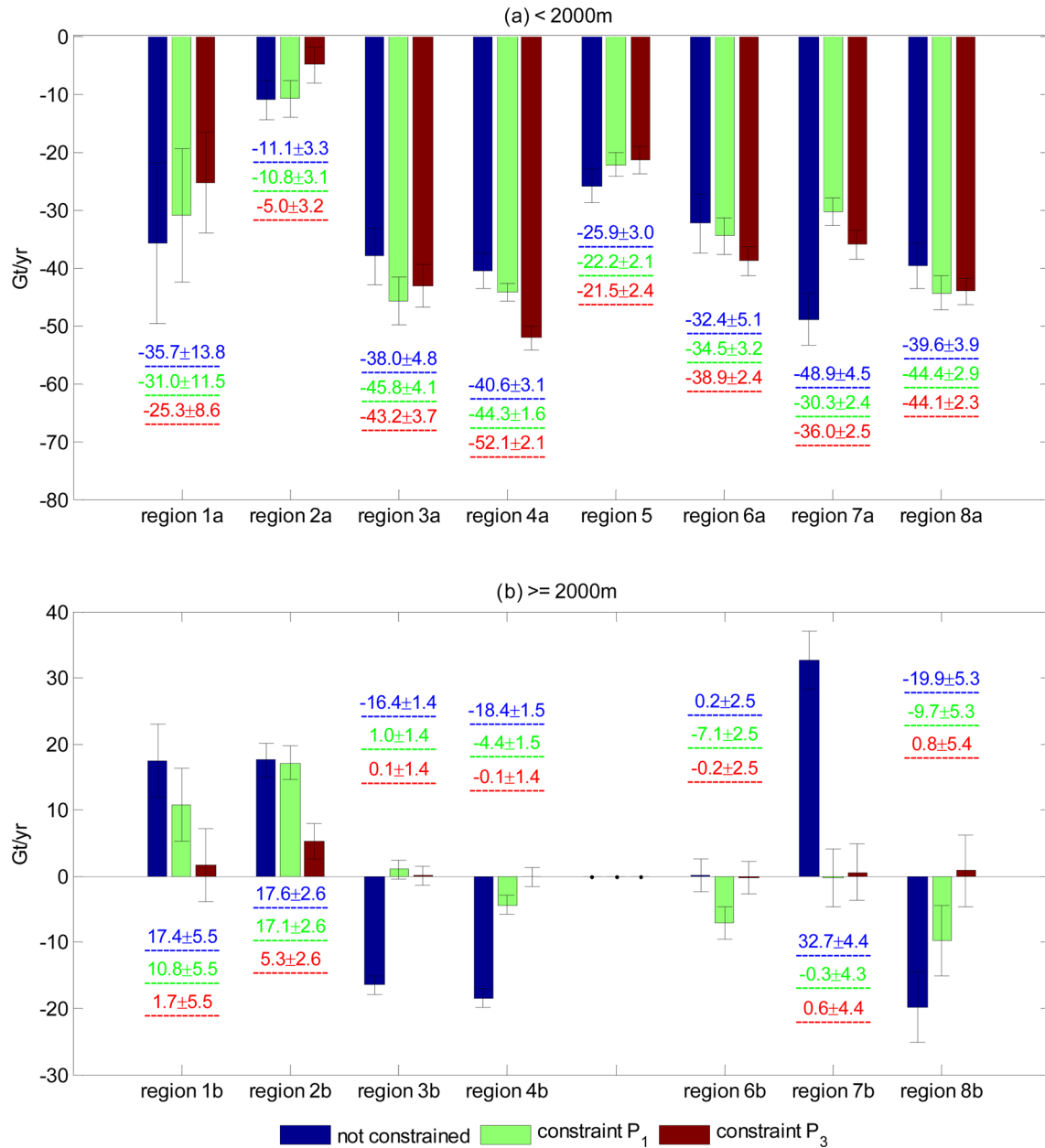


**Figure 6.** The annual mass change rates of the approximated GrIS regional solution for three different cases: unconstrained (blue), optimal  $P_1$  (green) and optimal  $P_3$  (red). The error bars include errors in the GRACE data, GIA model, GLDAS model as well as the errors caused by the linear interpolation.

constraints for regions below and above 2000 m. We are motivated to do this because the mass changes from the surface mass balance models clearly show smaller variance in regions above 2000 m than in the regions below 2000 m.

In order to determine the optimal  $P_3$  a model based simulation is employed, following BC13. We extended the optimization approach by adding as another objective function a measure of inter-region correlation of the regional mass balance from the output of the IOM model. By doing so the mass balance approximations in large areas yield a good agreement with similar regional GrIS studies. For example Luthcke *et al.* (2013) obtain approximated mass changes from December 2003 to December 2010 of  $-223.7 \pm 19.8$  Gt yr<sup>-1</sup> (for the margin regions) and  $-6.6 \pm 8.6$  Gt yr<sup>-1</sup> (for the interior regions). When applying the same time span, we find that the corresponding mass change trends constrained by  $P_3$  are  $-232.2 \pm 11.7$

and  $8.2 \pm 7.7$  Gt yr<sup>-1</sup>. Meanwhile we have successfully reduced anticorrelation errors caused by the oversensitivity of some regions, particularly in the GrIS interior. Thus, the use of separate constraints for higher parts of an ice sheet improves the regional mass balance estimates from GRACE. This suggests that our approach could also improve mass balance estimates for Antarctica where there are also regions of high and low mass variability.

When optimizing the constraints, we used an IOM model which comes with approximately 18 per cent uncertainty. We modify the output of the IOM model by removing (minimum scenario) or adding (maximum scenario) 18 per cent of the original EWT to investigate the influence of the IOM uncertainty during the optimization. When repeating the optimization procedure, we find that the optimal prior variances for the GrIS margin are 9.2 m<sup>2</sup> or 17.3 m<sup>2</sup>, for the minimum and maximum scenario, respectively.

However the changes of the constraints for the interior regions are less than  $0.02 \text{ m}^2$  compared to using the un-changed scenario in which the IOM model remains the same. The conclusion is that the optimization is more robust in the interior than in the margin, when considering the RACMO2 output and the discharge estimation as reference. The mass balance estimates only differ by  $0.9 \text{ Gt yr}^{-1}$  in the GrIS margin, and  $0.3 \text{ Gt yr}^{-1}$  in the interior regions from the original IOM. The differences are small when considering the uncertainties in the approximations, see the error bar in Fig. 6.

There are a few issues in the approach that can be further developed in future work:

(1) Even though we use three prior variances in the least-squares inversion, there are still differences between GRACE and the combination of modelled surface mass balance in RACMO2 and the estimated ice discharge in the west of Greenland, as can be seen in Fig. 2. In addition to distinguishing the regional mass changes between regions below and above 2000 m, different constraints can be used for the southern regions in the GrIS (region 4a–region 6a). However, this will add an extra unknown, and the method will rely more on prior knowledge. In addition, the method becomes computationally more demanding than for example the iterative forward modelling approach of W08.

(2) Another way to improve the regional mass changes approximation might be to introduce weights in the least-squares estimation. In eq. (5), we assume that each region in the system has equal weight. Thus a small area has the same weight as a larger area even though there are less observations that are sensitive to the smaller area. If we are able to properly weight all the regions in the system then the oversensitivity of smaller regions can become less significant.

## ACKNOWLEDGEMENTS

This research is funded by means of scholarship GO-AO/27 provided by the Netherlands Organization of Scientific Research, NWO. We are grateful to the Institute for Marine and Atmospheric research (IMAU), at Utrecht university for providing the RACMO2 model output for this study and to Ellyn Enderlin for providing the discharge estimates. Furthermore the authors acknowledge thoughtful comments by Oliver Baur and an anonymous reviewer of this manuscript.

## REFERENCES

- Andersen, M. *et al.*, 2015. Basin-scale partitioning of Greenland ice sheet mass balance components (2007–2011), *Earth planet. Sci. Lett.*, **409**, 89–95.
- Barletta, V.R., Sørensen, L.S. & Forsberg, R., 2013. Scatter of mass changes estimates at basin scale for Greenland and Antarctica, *Cryosphere*, **7**, 1411–1432.
- Baur, O. & Sneeuw, N., 2011. Assessing Greenland ice mass loss by means of point-mass modeling: a viable methodology, *J. Geod.*, **85**(9), 607–615.
- Bonin, J. & Chambers, D., 2013. Uncertainty estimates of a GRACE inversion modelling technique over Greenland using a simulation, *Geophys. J. Int.*, **194**, 212–229. (BC13)
- Chambers, D.P., 2006. Evaluation of new GRACE time-variable gravity data over the ocean, *Geophys. Res. Lett.*, **33**, L17603, doi:10.1029/2006GL027296.
- Chen, J., Rodell, M., Wilson, C. & Famiglietti, J., 2005. Low degree spherical harmonic influences on Gravity Recovery and Climate Experiment (GRACE) water storage estimates, *Geophys. Res. Lett.*, **32**, L14405, doi:10.1029/2005GL022964.
- Chen, J., Wilson, C., Famiglietti, J. & Rodell, M., 2007. Attenuation effect on seasonal basin-scale water storage changes from GRACE time-variable gravity, *J. Geod.*, **81**, 237–245.
- Chen, J., Wilson, C. & Tapley, B., 2011. Interannual variability of Greenland ice losses from satellite gravimetry, *J. geophys. Res.: Solid Earth*, **116**, doi:10.1029/2010JB007789.
- Cheng, M., Tapley, B.D. & Ries, J.C., 2013. Deceleration in the Earth's oblateness, *J. geophys. Res.: Solid Earth*, **118**, 740–747.
- Colgan, W., Abdalati, W., Citterio, M., Csatho, B., Fettweis, X., Luthcke, S., Moholdt, G. & Stober, M., 2013. Hybrid inventory, gravimetry and altimetry (HIGA) mass balance product for Greenland and the Canadian Arctic, *Cryosphere Dis.*, **8**, 537–580.
- Deb, K., Pratap, A., Agarwal, S. & Meyarivan, T., 2002. A fast and elitist multiobjective genetic algorithm: NSGA-II, *IEEE Trans. Evol. Comput.*, **6**, 182–197.
- Ettema, J., van den Broeke, M.R., van Meijgaard, E., van de Berg, W.J., Bamber, J.L., Box, J.E. & Bales, R.C., 2009. Higher surface mass balance of the Greenland ice sheet revealed by high-resolution climate modeling, *Geophys. Res. Lett.*, **36**, doi:10.1029/2009GL038110.
- Fang, H., Beaudoin, H. K., Rodell, M., Teng, W. L. & Vollmer, B. E., 2009. Global land data assimilation system (GLDAS) products, in *ASPRS 2009 Annual Conference*; 8–31 March, Baltimore, MD; USA.
- Fettweis, X., Tedesco, M., Broeke, M. & Ettema, J., 2011. Melting trends over the Greenland ice sheet (1958–2009) from spaceborne microwave data and regional climate models, *Cryosphere*, **5**, 359–375.
- Hamilton, G.S. & Whillans, I.M., 2002. Local rates of ice-sheet thickness change in Greenland, *Ann. Glaciol.*, **35**, 79–83.
- Hansen, P.C., 1992. Analysis of discrete ill-posed problems by means of the L-curve, *SIAM Rev.*, **34**, 561–580.
- Jacob, T., Wahr, J., Pfeffer, W.T. & Swenson, S., 2012. Recent contributions of glaciers and ice caps to sea level rise, *Nature*, **482**, 514–518.
- Johannessen, O.M., Khvorostovsky, K., Miles, M.W. & Bobylev, L.P., 2005. Recent ice-sheet growth in the interior of Greenland, *Science*, **310**, 1013–1016.
- Luthcke, S.B. *et al.*, 2006. Recent Greenland ice mass loss by drainage system from satellite gravity observations, *Science*, **314**, 1286–1289.
- Luthcke, S.B., Sabaka, T., Loomis, B., Arendt, A., McCarthy, J. & Camp, J., 2013. Antarctica, Greenland and Gulf of Alaska land-ice evolution from an iterated GRACE global mascon solution, *J. Glaciol.*, **59**, 613–631.
- MATLAB and Optimization Toolbox Release, 2012b. The MathWorks, Inc., Natick, Massachusetts, United States.
- Paulson, A., Zhong, S. & Wahr, J., 2007. Inference of mantle viscosity from GRACE and relative sea level data, *Geophys. J. Int.*, **171**, 497–508.
- Peltier, W., 2004. Global glacial isostasy and the surface of the ice-age Earth: the ICE-5G (VM2) model and GRACE, *Annu. Rev. Earth planet. Sci.*, **32**, 111–149.
- Ray, R. & Luthcke, S., 2006. Tide model errors and GRACE gravimetry: towards a more realistic assessment, *Geophys. J. Int.*, **167**, 1055–1059.
- Rignot, E. & Kanagaratnam, P., 2006. Changes in the velocity structure of the Greenland Ice Sheet, *Science*, **311**, 986–990.
- Rignot, E., Box, J., Burgess, E. & Hanna, E., 2008. Mass balance of the Greenland ice sheet from 1958 to 2007, *Geophys. Res. Lett.*, **35**, L20502, doi:10.1029/2008GL035417.
- Rodell, M. *et al.*, 2004. The global land data assimilation system, *Bull. Am. Meteorol. Soc.*, **85**, 381–394.
- Rowlands, D., Luthcke, S., McCarthy, J., Klosko, S., Chinn, D., Lemoine, F., Boy, J.P. & Sabaka, T., 2010. Global mass flux solutions from GRACE: a comparison of parameter estimation strategies—mass concentrations versus Stokes coefficients, *J. geophys. Res.: Solid Earth*, **115**, doi:10.1029/2009JB006546.
- Sasgen, I. *et al.*, 2012. Timing and origin of recent regional ice-mass loss in Greenland, *Earth planet. Sci. Lett.*, **333**, 293–303.
- Schrama, E.J. & Wouters, B., 2011. Revisiting Greenland ice sheet mass loss observed by GRACE, *J. geophys. Res.: Solid Earth*, **116**, doi:10.1029/2009JB006847. (SW11)
- Schrama, E., Wouters, B. & Vermeersen, B., 2011. Present day regional mass loss of Greenland observed with satellite gravimetry, *Surv. Geophys.*, **32**, 377–385.



- Schrama, E.J., Wouters, B. & Rietbroek, R., 2014. A mascon approach to assess ice sheet and glacier mass balances and their uncertainties from GRACE data, *J. geophys. Res.: Solid Earth*, **119**, 6048–6066.
- Shepherd, A. *et al.*, 2012. A reconciled estimate of ice-sheet mass balance, *Science*, **338**, 1183–1189.
- Swenson, S. & Wahr, J., 2002. Methods for inferring regional surface mass anomalies from Gravity Recovery and Climate Experiment (GRACE) measurements of time variable gravity, *J. geophys. Res.: Solid Earth*, **107**, ETG 3-1–ETG 3-13.
- Swenson, S. & Wahr, J., 2006. Post-processing removal of correlated errors in GRACE data, *Geophys. Res. Lett.*, **33**, L08402, doi:10.1029/2005GL025285.
- Swenson, S. & Wahr, J., 2007. Multi-sensor analysis of water storage variations of the Caspian Sea, *Geophys. Res. Lett.*, **34**, L16401, doi:10.1029/2007GL030733.
- Swenson, S., Wahr, J. & Milly, P., 2003. Estimated accuracies of regional water storage variations inferred from the Gravity Recovery and Climate Experiment (GRACE), *Water Resour. Res.*, **39**, doi:10.1029/2002WR001808.
- Swenson, S., Chambers, D. & Wahr, J., 2008. Estimating geocenter variations from a combination of GRACE and ocean model output, *J. geophys. Res.: Solid Earth*, **113**, doi:10.1029/2007JB005338.
- Thomas, R., Csatho, B., Davis, C., Kim, C., Krabill, W., Manizade, S., McConnell, J. & Sonntag, J., 2001. Mass balance of higher elevation parts of the Greenland ice sheet, *J. geophys. Res.: Atmos.*, **106**, 33 707–33 716.
- Tikhonov, A.N., 1963. Regularization of incorrectly posed problems, *Soviet Math. Dokl.*, **4**, 1624–1627.
- van den Broeke, M. *et al.*, 2009. Partitioning recent Greenland mass loss, *Science*, **326**, 984–986.
- Velicogna, I., 2009. Increasing rates of ice mass loss from the Greenland and Antarctic ice sheets revealed by GRACE, *Geophys. Res. Lett.*, **36**, doi:10.1029/2009GL040222.
- Velicogna, I. & Wahr, J., 2005. Greenland mass balance from GRACE, *Geophys. Res. Lett.*, **32**, doi:10.1029/2005GL023955.
- Velicogna, I. & Wahr, J., 2006. Measurements of time-variable gravity show mass loss in Antarctica, *Science*, **311**, 1754–1756.
- Velicogna, I. & Wahr, J., 2013. Time variable gravity observations of ice sheet mass balance: precision and limitations of the GRACE satellite data, *Geophys. Res. Lett.*, **40**, 3055–3063.
- Vernon, C., Bamber, J., Box, J., Van den Broeke, M., Fettweis, X., Hanna, E. & Huybrechts, P., 2013. Surface mass balance model intercomparison for the Greenland ice sheet, *Cryosphere*, **7**, 599–614.
- Wahr, J., Molenaar, M. & Bryan, F., 1998. Time variability of the Earth's gravity field: hydrological and oceanic effects and their possible detection using GRACE, *J. geophys. Res.*, **103**, 30 205–30 230.
- Wouters, B., Chambers, D. & Schrama, E., 2008. GRACE observes small scale mass loss in Greenland, *Geophys. Res. Lett.*, **35**, doi:10.1029/2008GL034816.
- Zwally, H.J., Giovinetto, M.B., Li, J., Cornejo, H.G., Beckley, M.A., Brenner, A.C., Saba, J.L. & Yi, D., 2005. Mass changes of the Greenland and Antarctic ice sheets and shelves and contributions to sea-level rise: 1992–2002, *J. Glaciol.*, **51**, 509–527.
- Zwally, H.J. *et al.*, 2011. Greenland ice sheet mass balance: distribution of increased mass loss with climate warming; 2003–07 versus 1992–2002, *J. Glaciol.*, **57**, 88–102.
- Zwally, H.J., Giovinetto, M.B., Beckley, M.A. & Saba, J.L., 2012. *Antarctic and Greenland Drainage Systems*, GSFC Cryospheric Sciences Laboratory. Available at: [http://icesat4.gsfc.nasa.gov/cryo\\_data/ant\\_grn\\_drainage\\_systems.php](http://icesat4.gsfc.nasa.gov/cryo_data/ant_grn_drainage_systems.php), last accessed 30 March 2015.